Buckling of single-walled carbon nanotubes upon bending: Molecular dynamics simulations and finite element method

Guoxin Cao and Xi Chen*
Nanomechanics Research Center, Department of Civil Engineering and Engineering Mechanics, Columbia University, New York, New York 10027, USA
(Received 10 January 2006; published 27 April 2006)

The bending buckling behaviors of single-walled carbon nanotubes (SWCNTs) are systematically investigated by using both molecular dynamics (MD) simulation and finite element method (FEM), to analyze the relationships between critical bending buckling curvature, critical buckling strain and nanotube geometry parameters (e.g., tube diameter, length and chirality). The postbuckling shape of SWCNT and the effect of loading boundary conditions are also discussed. The comparison between MD and FEM simulations shows that the continuum shell model provides some useful insights into the bending buckling mechanisms, yet it cannot quantitatively reproduce the bending buckling behavior of SWCNTs, since the continuum model does not account for the geometrical imperfections in the atomic system that are critical to the onset of buckling. Improvements of continuum models are suggested based on the findings.

DOI: 10.1103/PhysRevB.73.155435 PACS number(s): 65.80.+n, 61.48.+c, 61.50.Ah, 81.07.De

I. INTRODUCTION

Carbon nanotubes (CNTs) have been subjected to intensive study since their discovery in 1991 due to their unique combinations of mechanical, electrical and chemical properties.[1–5] In order to fulfill their promising applications such as nanostrain sensors and actuators, nanofluidic components, and carbon nanotube-reinforced composites, the mechanical properties of CNTs must be fully understood. A variety of experimental works have been put together to investigate the elastic properties of CNTs, focusing on Young's moduli. Treacy and co-workers have pioneered the measurement of thermally induced vibration amplitudes of CNT cantilevers from 20 to 800 °C: for multi-walled carbon nanotubes (MWCNTs) and single-walled carbon nanotubes (SWCNTs), the effective Young's moduli of reported to be in the ranges of 0.40–4.15 TPa[6] and 0.9–1.9 TPa,[7] respectively. Alternatively, by using an atomic force microscope (AFM) tip to bend a MWCNT cantilever, the Young's moduli of MWCNTs are found to be 1.28±0.59 TPa.[8]

Besides the studies of CNT elastic properties at small deformation, the mechanical response of CNTs under large deformation has begun to receive wide attention: in particular, the buckling behaviors of CNTs subjecting to excess deformation have been observed.[1,9,10] Experimental investigations have also shown that the buckling deformation of CNTs under very large strain can be completely recovered after unloading.[9,11,12] It is found that the physical properties such as conductance of CNTs are strongly influenced by the occurrence of buckling.[13] Thus, the reversible transformation between the buckled state and normal state of CNTs may lead to potential applications such as nano-electronic devices (nano-transistors),[13] nano-fluid components (nano-valve)[14] and reversible elements in nano-electromechanical systems. In view of both mechanical integrity and application, it is very important to understand the buckling mechanisms of CNTs.

The experimental investigation of buckling behavior of CNTs remains a challenge because of difficulties encountered at the nano-scale.[9] For that matter, both theoretical and numerical approaches have been used to explore the buckling behavior of CNTs, which can be divided into three main categories: (1) Atomistic simulations based on the molecular dynamics (MD);[10,15–22] (2) continuum mechanics modeling where the CNTs are effectively modeled as continuous beams or thin shells with a fixed wall thickness, Young's modulus and Poisson's ratio;[15,23–30] (3) analytical modeling based on molecular structural mechanics,[31–33] discussed below.

With the development of more accurate force field and numerical algorithms, MD simulations have been shown to play an important role in revealing the mechanical behavior of CNTs. Yakobson, Brabec, and Bernholc[15] studied the buckling behavior of SWCNTs under axial compression, bending and torsion. Their results suggested that the critical buckling strain under axial compression is inversely proportional to the tube diameter, and the critical bending buckling curvature under bending deformation varies as inverse square of the SWCNT diameter. The critical buckling strains of bending and axial compression are assumed to be equal in Yakobson's study,[15] examined in detail below. Buehler, Kong, and Gao[17] investigated the length dependence of critical buckling strain of SWCNTs under axial compression and reported that the buckling behavior depends strongly on tube length: the critical buckling strain decreases with increasing CNT length/diameter aspect ratio. Iijima *et al.*[10] simulated the bending behavior of SWCNTs with varying lengths, diameters and chiralities and showed that the critical bending buckling curvature is independent of the tube length. Liew *et al.*[16] investigated buckling behavior of SWCNTs and MWCNTs (including two-, three-, and four-walled nanotubes) under axial compression and compared different buckling behaviors between SWCNTs and MWCNTs. Srivastava and Barnard[22] studied axial buckling of a (10,10) SWCNT and a $(5n,5n)_{n=4-7}$ MWCNT by MD. At present, most MD simulations of buckling behavior of CNTs are focused on axial compression. A systematic MD study on the bending

buckling behaviors of CNTs is still lacking. Furthermore, compared with axial compression, bending buckling is much easier to realize and control in practical applications, such as nano-valve[14] or nano-transistor.[13] This is the main motivation of the present study.

Although MD simulations yield explicit results in many cases, due to the limitation in time scales (typically several ns or less) and length scales, they become less practical in investigating the buckling characteristics of long CNTs, MWCNTs, or CNT bundles involving a large number of atoms. As an alternative, the simple continuum shell model is used to investigate buckling behavior of CNTs,[15,23–31] which includes both analytical solution of thin shell buckling and FEM analysis of the tube response under large compressive strain. Since the phenomenological shell model does not incorporate discrete atomic features, analytical models based on the molecular structural mechanics have also been developed to study the mechanical behaviors of CNTs.[31–33] This method is based on equating the molecular potential energy in MD with mechanical strain energy in an equivalent continuum or structural mechanics model. It still remains unclear whether these continuum or structural mechanics-based models may accurately predict the critical strain of CNT bending buckling.

A systematic and relatively complete set of MD simulations on the bending buckling behaviors of SWCNTs would provide critical insights into the buckling mechanisms and to improve the continuum mechanics modeling. For instance, Yakobson, Brabec, and Bernholc[15] have argued that the snap buckling during bending is a "local" shell-like behavior, thus, the critical buckling strain under bending deformation should be equal to that under axial compression—this assumption, however, has not yet been verified. Is bending buckling merely a local behavior that is equivalent to axial compression? How do the critical bending buckling curvature and postbuckling shape vary with the length, diameter and chirality of SWCNTs? Can the continuum model be employed to predict the onset of bending buckling? These are all important questions that need to be addressed.

In this study, the buckling behaviors of SWCNTs under bending deformation are investigated by comprehensive MD simulations and FEM analyses based on the thin shell model. The effects of tube length, diameter and chirality are systematically studied. The relationships between critical bending buckling curvature and geometrical parameters of SWCNTs are established. Comparisons between MD and FEM results yield important insights into the buckling mechanisms, effect of loading boundary conditions, and disadvantages of continuum modeling. The findings of this paper may provide useful information for the mechanical integrity and application of buckled CNTs in practice.

II. COMPUTATION METHODS

A. Molecular dynamics simulations

With the recent development of more accurate force field, molecular dynamics (MD) becomes a powerful tool to simulate CNT behaviors at the nano-scale. In this paper, atomic interactions in the CNT system are modeled by using the COMPASS force field, (condensed-phased optimized molecular potential for atomistic simulation studies), the first and only *ab initio* force field that enables an accurate and simultaneous prediction of various gas-phase and condensed-phase properties of organic and inorganic materials.[34] All computations are carried out at 0 K.

In the present work, eight different armchair and zigzag SWCNTs with the same length are selected to study the effect of tube diameter on bending buckling behaviors. In order to explore the effect of chirality, we choose pairs of armchair and zigzag types of nanotubes with radii that are closely matched with each other. The armchair-type nanotubes used in this study are (5,5), (10,10), (15,15) and (20,20), respectively, and the zigzag type nanotubes employed are (9,0), (17,0), (26,0) and (35,0), respectively. The lengths of all SWCNTs are set to be roughly equal, about 24 nm. The armchair tubes include 100 periodic lengths, and zigzag tubes include 58 periodic lengths; there is about less than 0.5% of tube length difference between armchair and zigzag tubes due to their different periodic lengths.

In order to show the effect of nanotube length on the buckling characteristics, we studied the buckling of (9,0) and (5,5) SWCNTs under axial compression and bending deformation, with their lengths varying from about 4 to 35 nm. Note that the radius of (9,0) and (5,5) are very close, thus, the comparison between them also infers the influence of chirality.

Within the Cartesian coordinate system, the axis of the SWCNT is aligned with the x_2 axis, and bending occurs within the x_1-x_2 plane (cf. Figs. 5 and 6). Prior to deformation, the initial atomic structure of SWCNT is optimized by the molecular mechanics method, such that the total potential energy is minimized and forces between atoms are zero. To apply bending deformation, rigid body translation is applied to the atoms in both end layers of SWCNT, such that both end sections remain circular and are kept perpendicular to the deformed axis in each displacement increment; the length of the deformed tube axis remains unchanged and its curvature is essentially uniform throughout deformation. Such displacement-controlled loading is widely used in literature to simulate the pure bending deformation of SWCNTs in MD.[10,15,18] During each small displacement increment, the carbon atoms in both end layers are first moved to and fixed at their new positions, then, all other carbon atoms relocate to their new equilibrium positions by minimizing the potential energy of the whole system.

In order to pinpoint the critical bending buckling curvature, the system strain energy computed from MD simulation, U_{bend}^{MD}, is a function of the bending angle (i.e., the angle corresponding to the deformed arc of the tube axis), θ. With the increase of θ, initially, U_{bend}^{MD} scales with θ^2. Once snap buckling is initiated, the derivative of U_{bend}^{MD} with respect to θ decreases abruptly. Denote the critical angle by θ_{cr}, the critical bending buckling curvature of deformed axis computed from MD is $\kappa_c \equiv \kappa_{cr\text{-}bend}^{MD} = \theta_{cr}/L$, with L the SWCNT length. When the tube deformation is pure bending, the axial strain is uniform along the longitudinal line with largest curvature, and the critical bending buckling strain is $\varepsilon_c \equiv \varepsilon_{cr\text{-}purebend}^{MD} = \kappa_{cr\text{-}bend}^{MD} \cdot d/2$ with d the tube diameter. Both critical bending buckling curvature and strain are used to describe the threshold of bending buckling, discussed below.

B. Continuum shell modeling

The buckling behaviors of SWCNTs under axial compression have been investigated by using the continuum shell model and beam model.[15,17] When the aspect ratio of SWCNT, which is defined as the ratio between the tube length, L, and the tube diameter, d, is larger than 50, the mechanical behavior of SWCNTs approaches that of a beam. The critical buckling strain of a compressed beam with both ends clamped is

$$\varepsilon_{cr\text{-}comp}^{beam} = (\pi d/L)^2/2, \tag{1}$$

which is independent of the tube wall thickness, t ($t \ll d$). With increasing tube length, the critical compressive buckling strain decreases rapidly. On the other hand, for SWCNTs with small aspect ratio, their mechanical behaviors are close to that of thin shells. The critical compressive buckling strain of a cylindrical thin shell under axial compression can be described as[35]

$$\varepsilon_{cr\text{-}comp}^{shell} = \frac{2}{\sqrt{3(1-\nu^2)}}\frac{t}{d} \approx 1.176\frac{t}{d}, \tag{2}$$

where the Poisson's ratio of graphite, $\nu=0.19$, is taken for the CNTs. The critical compressive buckling stain of an axishell is proportional to shell thickness and independent of the tube length.

The snap buckling behavior of SWCNTs under bending deformation is more complicated. Snap buckling does not occur in beams; for thin shells, Yakobson, Brabec, and Bernholc[15] assumed that the local critical strain of snap buckling equals the critical buckling strain of axial compression (2). Under such assumption, the critical bending buckling curvature can be described as

$$\kappa_{cr\text{-}bend}^{Yakobson} = 2\varepsilon_{cr\text{-}comp}^{shell}/d = 2.352 \cdot t/d^2. \tag{3}$$

The critical bending buckling curvature is independent of the tube length and it scales with t/d^2. By studying the elastic properties of a (13,0) SWCNT with length 8 nm and diameter 1 nm, Yakobson, Brabec, and Bernholc[15] have obtained an effective shell thickness, $t=0.066$ nm.

In order to gain more insights into the buckling mechanisms and to explore whether the continuum shell model can be applied to quantitatively predict the critical bending buckling curvature, in this paper, FEM analyses are also employed to study the bending buckling behavior of thin cylindrical shells with varying length, radius and wall thickness. In finite element simulation, the general-purpose shell element (S4R) is adopted in ABAQUS analysis, which provides robust and accurate finite strain solutions in all loading conditions regardless of the thickness of the shell.[36] A typical mesh of SWCNT comprises more than 10 000 four-node elements with reduced integration. Convergence analyses have been used to justify the mesh density in all simulations. An effective Young's modulus 6.85 TPa is used in FEM simulations based on our recent work[28]—it should be noted that from dimensional analysis, it is straightforward to show that both critical bending buckling strain and curvature are independent of the elastic modulus of the tube. The bending is displacement controlled and the boundary conditions are identical to those applied in MD simulation. Again, the deformed tube axis is within the x_1-x_2 plane (cf. Figs. 7 and 8). In FEM analyses, the critical bending buckling strain ε_c^{FEM} (in the deformed axial direction) and critical bending buckling curvature κ_c^{FEM} are computed in a way that is similar to the MD procedure described above, and compared with their MD counterparts ε_c and κ_c, respectively.

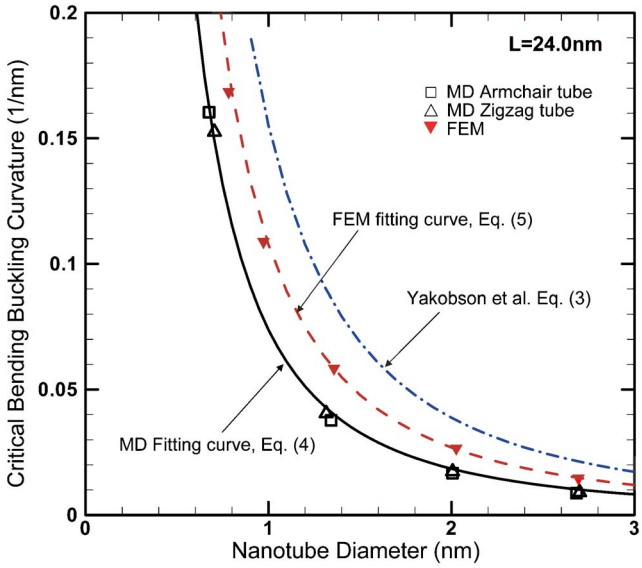

FIG. 1. (Color online) The relationships between critical bending buckling curvature and nanotube diameter. Results computed from MD and FEM analyses are compared with the model by Yakobson and co-workers.[15] The tube length is fixed at 24 nm.

III. RESULTS AND DISCUSSIONS

A. Effects of diameter and chirality on critical bending buckling curvature

From MD simulations, the relationships between the critical bending buckling curvature (κ_c) and nanotube diameter (d) are shown as open symbols in Fig. 1, all tubes with the same length, $L \approx 24$ nm. The relationship between critical bending buckling curvature and nanotube diameter can be fitted as

$$\kappa_c = a/d^2 \quad \text{with } a = 0.0738 \text{ nm}, \tag{4}$$

where the unit of d is nanometer and the unit of κ_c is 1 nm; the fitted function is plotted as solid line in Fig. 1. It can be readily seen that for all different SWCNTs with same length, κ_c drops off as inverse square of the tube diameter and such relationship is insensitive to the chirality of nanotube. The effect of tube length will be investigated in the next section.

Equation (4) is fitted from MD simulations, which has a very similar functional form as the one proposed by Yakobson and co-workers,[15] i.e., Eq. (3). With $t=0.066$ nm, Eq. (3) can be rewritten as $\kappa_{cr\text{-}bend}^{Yacobson} = a^Y/d^2$ (1 nm) with a different coefficient, $a^Y=0.155$ nm which is about twice our result. This is also plotted in Fig. 1 as the dash-dot curve—comparing with out MD results, Yakobson and co-workers[15]

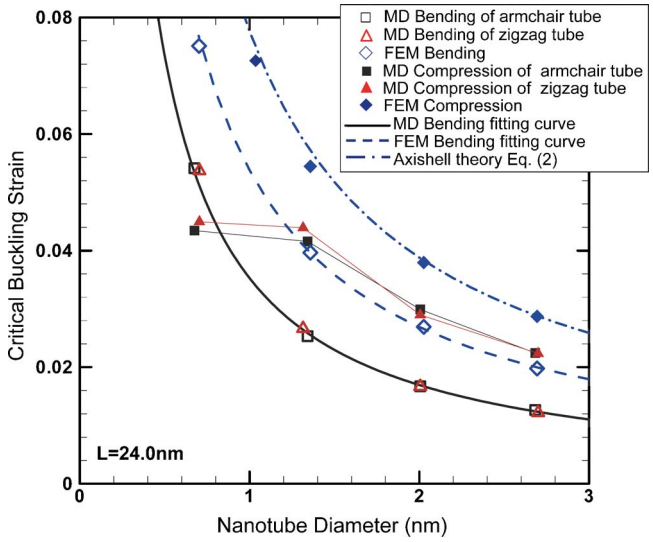

FIG. 2. (Color online) The comparison between the critical buckling strains of bending and axial compression of SWCNTs with same length (24 nm). Both MD and FEM results are presented and compared with the axishell theory for compression.

have significantly overestimated the critical bending buckling curvature. In Yakobson's model, since the critical bending buckling strain was set to be equal to the critical buckling strain of axishell compression (2), the derived critical bending buckling curvature (3) is strictly independent of tube length. However, by using MD simulation, Liew *et al.*[16] have studied the critical buckling strain of (10,10) SWCNT under axial compression, and their results showed that the critical compressive buckling strain decreases when the tube length is increased from 2.46 to 14 nm. This evidence suggests that it is problematic to assume the critical bending buckling strain equals the critical compressive buckling strain.

To further examine the relationship between critical buckling strains of bending and axial compression, we also simulated the buckling behaviors of all eight different tubes under axial compression (with both ends "clamped") using MD simulation. Figure 2 compares the axial compression and bending critical buckling strains of armchair and zigzag tubes with the same length. When tube diameter is relatively large, $d>1.3$ nm, the ratio between the critical bending buckling strain $\varepsilon_c \equiv \varepsilon^{MD}_{cr\text{-}purebend}$ and the critical compressive buckling strain $\varepsilon^{MD}_{cr\text{-}comp}$ is nearly a constant, about 0.6. On the other hand, for smaller SWCNTs such as (5,5) and (9,0), $\varepsilon^{MD}_{cr\text{-}purebend}/\varepsilon^{MD}_{cr\text{-}comp}$ increases to about 1.2—the effect of aspect ratio L/d will be discussed in next section. Therefore, the critical buckling strains of bending and compression are distinct.

In order to gain more insights, we have also carried out a set of FEM simulations to explore the buckling characteristics by varying the nanotube diameter, d. The length of cylindrical shell is fixed at $L=24$ nm. To compare with the work by Yakobson and co-workers,[15] the shell thickness is taken to be $t=0.066$ nm. The relationship between κ_c^{FEM} and d is plotted in Fig. 1 as solid symbols, which can be readily fitted by the dash curve

$$\kappa_c^{FEM} = a^{FEM}/d^2 \quad \text{with } a^{FEM} = 0.1076 \text{ nm}. \tag{5}$$

Compared with MD, the FEM simulation also overestimates the critical bending buckling curvature. The reason is the following: in FEM analysis, the tube is a perfect cylindrical continuum shell without any imperfection, whereas in the MD simulation, the SWCNT is a cluster of discrete carbon atoms that are distributed on a cylindrical surface. The precise coordinates of every carbon atom in SWCNT are determined by the minimization of the total potential energy. Due to the complicated force field, the energy minimization may not lead to a perfect symmetric distribution of all atoms, and small local geometrical imperfections are inevitable. Note that such geometrical imperfections (with respect to an ideal perfect cylindrical shell) are uniformly distributed in the nanotubes, which is also one of the intrinsic geometrical characteristics of the SWCNTs. Therefore, the geometrical imperfections, which are fundamentally different than the defects such as atomic vacancies or the Stone Wales defect (i.e., pentagon and heptagon pair by rearrangement of the bonds), do not tend to cause any unpredictable experimental results. Nevertheless, owing to the fact that the onset of buckling is very sensitive to the perturbation imposed by small imperfections, the critical bending buckling curvature obtained from MD simulation is smaller than that from FEM analysis. Therefore, the imperfection-free continuum model cannot be used to accurately determine the critical bending buckling curvature.

We note that the imperfections are important only during the buckling bifurcation analysis involving large strains, whereas the effect of structural imperfection is negligible in most small strain applications. Therefore, the simple continuum shell model can be applied to describe the CNT tension, bending, and torsion behaviors at small deformation, from which the nanotube elastic properties such as the Young's modulus can be readily obtained—the success of such have been demonstrated by many previous studies.[15,23–31] Despite its inherent disadvantage, with reference to Fig. 1, the continuum shell model is still capable of predicting that the critical bending buckling curvature scales with $1/d^2$. This implies that the overall effect of geometrical imperfection can be reduced into a factor, which equals to $e^{shell}=a/a^{FEM}=0.686$. After incorporating such correction factor, the critical bending buckling curvature computed from the continuum analyses becomes $e^{shell}a^{FEM}/d^2$, which agrees well with MD simulation when the tube length is fixed at 24 nm. The effects of SWCNT length will be discussed below.

FEM simulations of axial compression of nanotubes (with fixed L and t) are also performed, and the calculated critical buckling strains of bending and compression are compared in Fig. 2: both are higher than MD results where the imperfections are playing a critical role. For axial compression, the critical buckling strain computed from FEM ($\varepsilon^{FEM}_{cr\text{-}comp}$, solid diamond) is very close to the axishell theory, i.e., Eq. (2) ($\varepsilon^{shell}_{cr\text{-}comp}$, the dash-dot curve). Within the framework of the imperfection-free continuum model, the critical bending buckling strain is about 69% of its compressive counterpart for all tube diameters studied in this paper, which indicates

that bending buckling is much easier to occur than the compressive bucking of axishell. Indeed, these two are distinct bifurcation modes: the postbuckling shape of axishell under compression remains axisymmetric and all cross sections remain circular; by contrast, the tube sections away from the end become elliptical during bending. Moreover, the compressive axial stress is applied uniformly on the cross section of an axishell, whereas during bending the gradients of both axial and hoop stresses across the tube section are large—all these factors make the tube much easier to buckle under bending (with respect to the long axis of the deformed elliptical section).

When the tube is modeled as a cylindrical shell with fixed length, the critical bending buckling curvature is smaller if the wall is thicker. Since $\kappa_c^{FEM}=a^{FEM}/d^2$, from dimensional analysis, a^{FEM} must be proportional to t, which leads to

$$\kappa_c^{shell} \cong \kappa_c^{FEM} = bt/d^2 \quad \text{with } b = 1.63. \tag{6}$$

This universal relationship for cylindrical shells will be verified by FEM analyses with varying t and L in the next section. When $t=0.066$ nm,[15] $bt=0.1076$ nm. On the other hand, in order to match the continuum analysis with MD simulation, the effective shell thickness should be $t^{eff}=a/b=0.045$ nm. In the previous continuum shell models known to the authors, the effective SWCNT wall thickness is reported in the range from 0.066 to 0.089 nm.[15,24,28,37–39] Therefore, when compared with MD benchmarks, even the smallest wall thickness in the literature ($t=0.066$ nm) will cause about 45% error of critical bending buckling curvature, and such error may be overcome by using the correction factor to account for the effect of geometrical imperfections, discussed above.

B. Effect of nanotube length on critical bending buckling curvature

From MD simulations of the bending of SWCNTs with varying lengths, diameters and chiralities, Iijima *et al.*[10] reported that the critical bending buckling curvature is independent of the tube's length L. However, the work by Liew *et al.* on axial compression,[16] as well as our MD results on bending in Fig. 2, suggest that the length/diameter aspect ratio of SWCNTs also affects the critical buckling behavior. In this section, we first study the bending buckling behavior of (9,0) SWCNTs with different lengths by using MD simulation, and the variation of κ_c with L/d is shown in Fig. 3. The results show that the variation of κ_c is less than 4% when the nanotube aspect ratio $L/d=10-50$, which is essentially length insensitive; on the other hand, when $L/d<10$, κ_c decreases for about 20% when L/d reduces from roughly 10 to 6. Note that the aspect ratio used in the work of Yakobson, Brabec, and Bernholc,[15] $L/d=8$, is within such length-dependent region. Whereas, the aspect ratio of SWCNTs used in the work of Iijima *et al.*[10] may be inside the length-insensitive region since they did not specify the aspect ratio used in their work.

In order to further explore the effect of chirality, the bending buckling behavior of armchair SWCNT (5,5) is studied next, with varying tube lengths. The $\kappa_c \sim L/d$ relationship of

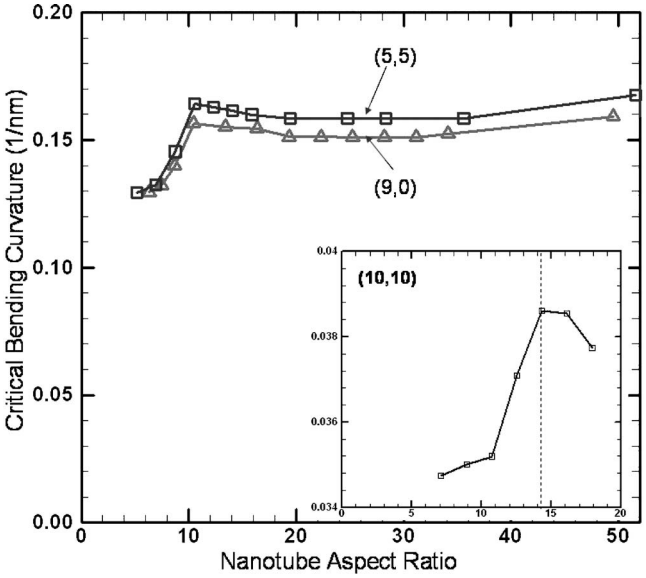

FIG. 3. The length dependence of critical bending buckling curvature of (5,5), (9,0) and (10,10) tubes.

(5,5) SWCNT has the same trend as that of (9,0) tube, where κ_c becomes length dependent once $L/d<10$ and such property is not affected by the chirality. Thus, a threshold aspect ratio of about 10 is found when $d \approx 0.7$ nm.

The inset of Fig. 3 shows the length dependence of critical bending buckling curvature for tube (10,10). Although the trends are similar, with decreasing L/d, the magnitude of κ_c reduction of (10,10) is less than that of (5,5): for (10,10), κ_c is reduced about 10% when L/d reduces from 14 to 7. Moreover, the threshold aspect ratio is about 14 for (10,10) SWCNT, which is larger than that of (5,5) and (9,0) tubes. Therefore, the threshold L/d below which κ_c becomes length dependent, is governed by the tube radius and not by chirality: for tubes with large radii, such threshold aspect ratio is larger, and the reduction of κ_c is less apparent, as demonstrated in Fig. 1. To better understand the mechanism of the length-dependent κ_c when L/d is below a threshold, the geometrical structure of pre- and postbuckling SWCNTs needs to be explored, elaborated in the next section.

Systematic FEM analyses are also carried out on SWCNT bending buckling by varying the aspect ratio, L/d, wall thickness, t, and the Young's modulus, E. The results are presented in Fig. 4. It is found that the critical bending buckling curvature κ_c is insensitive to the tube length within the framework of shell model. For the wide range of parameters used in this study, the universal continuum relationship Eq. (6) fits all numerical results. On one hand, since the continuum shell model has no length dependence, it may not be used to accurately represent the buckling characteristics of all SWCNTs. On the other hand, if the tube radius is relatively large, the length dependence becomes less obvious; thus, when either the correction factor e^{shell} (with $t=0.066$ nm) or the effective shell thickness $t^{eff}=0.045$ nm is used, the phenomenological shell model still does a reasonably good job of describing the overall bending buckling behavior of nanotubes.

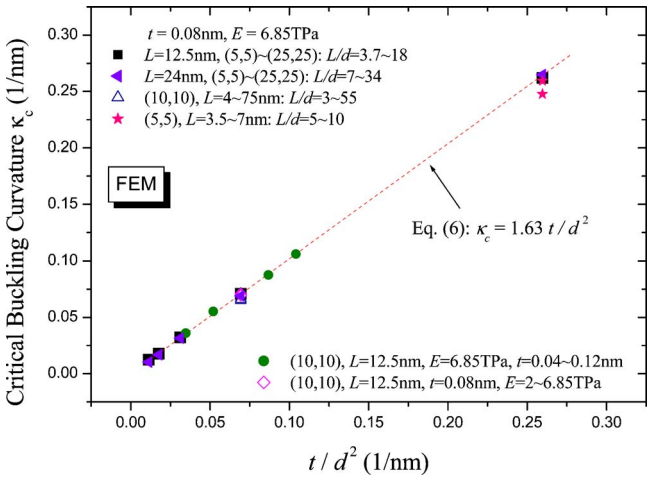

FIG. 4. (Color online) The relationship between critical bending buckling curvature and nanotube geometrical parameters established from FEM analysis.

C. Geometrical structure of buckled SWCNTs

From the results displayed in Fig. 3, we can see that κ_c sharply decreases when the aspect ratio, L/d, of (9,0) decreases from 10.5 to 8.7. The geometrical structure of (9,0) tubes at the onset of buckling, with $L/d=8.7$ ($L=6.11$ nm) and $L/d=10.5$ ($L=7.36$ nm), are shown in Figs. 5(a) and 5(b), respectively. The buckled structures are distinct: there is only one snap buckle located in the middle of the tube for $L/d=8.7$, whereas two symmetrical snap buckles are found simultaneously near the end of SWCNT with $L/d=10.5$: the distance between the buckle and the end is about 5 periodic lengths (2.08 nm).

By contrast, two longer (9,0) tubes with aspect ratios $L/d=25.2$ ($L=17.78$ nm) and $L/d=49.5$ ($L=34.86$ nm) are shown in Figs. 5(c) and 5(d), respectively. For $L/d=25.2$, there are also two symmetrical snap buckling positions that are about 5.5 periodic lengths (2.29 nm) from the end. Thus, for tubes with two snap buckling positions, the distance between the kink and tube end increases slightly with increasing L. For the longest tube with $L/d=49.5$, five buckles appeared at the same time: one of them is located in the middle of the tube, and the other four are biased to the end. The distance between the nearest and next nearest buckling positions and the tube end is about 8 periodic lengths (3.33 nm) and 18 periodic lengths (7.5 nm), respectively.

For (9,0) SWCNT, when L/d is reduced from 10.5 to 8.7, the buckled shape changes from two kinks [Fig. 5(b)] to one kink [Fig. 5(a)], which may have caused the critical bending buckling curvature to sharply reduce (Fig. 3). It appears that the critical bending buckling curvature of (9,0) SWCNT is sensitive to tube length if only one snap buckle is developed, and κ_c becomes length insensitive if the buckled geometry contains more than one kink. Further MD geometry analyses show that the buckled structure of (9,0) tube has one kink when $L/d \leqslant 8.7$, and two kinks when $L/d \geqslant 10.5$. More kinks will likely develop for tubes with large L/d: for instance, five kinks are found when $L/d=49.5$ [Fig. 5(d)], yet that does not affect κ_c in a significant way (Fig. 3).

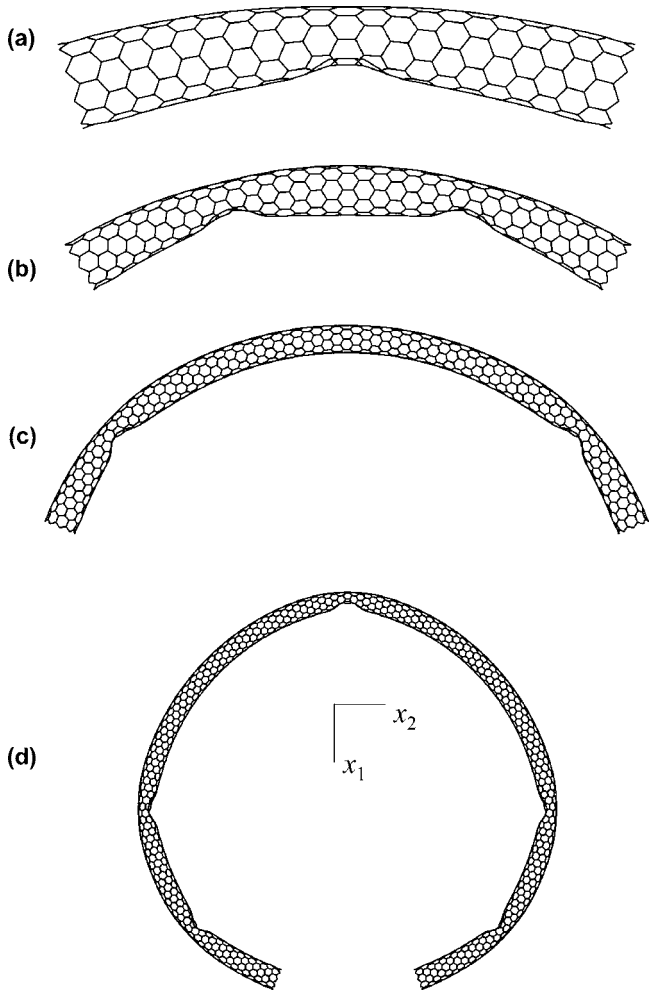

FIG. 5. The geometry of (9,0) tubes at the onset of bending buckling with different lengths: (a) $L=6.11$ nm, (b) $L=7.36$ nm, (c) $L=17.78$ nm, and (d) $L=34.86$ nm.

The configurations shown in Fig. 5 are recorded at the onset of buckling. With further increase of the bending curvature of (9,0) tube, if $L/d \leqslant 8.7$, the postbuckling shape will change from one snap buckle in the middle to two symmetric kinks near the end; meanwhile, for tubes with moderate length ($L/d \geqslant 10.5$), an extra kink will appear at the middle following the formation of two snap buckles near the end.

When the postbuckling shapes of SWCNTs with different diameters and same length ($L=24$ nm) are compared in Fig. 6, it is found that (35,0) and (26,0) tubes have one kink in the middle, but the smaller (17,0) and (9,0) tubes have two symmetrical snap buckles near the end. Therefore, it is confirmed that the buckled geometry is governed by the aspect ratio of tube, L/d. In general, if L/d is less than 10 or so, the postbuckling shape has one kink, and two or more snap buckles are likely to develop in tubes with larger aspect ratios. Further studies have shown that the armchair SWCNTs have similar characteristics to those shown in Figs. 5 and 6 or zigzag nanotubes. For simplicity, we just show the results of zigzag tubes.

These observations are in general agreement with the literature. Iijima *et al.*[10] also reported that upon further bending

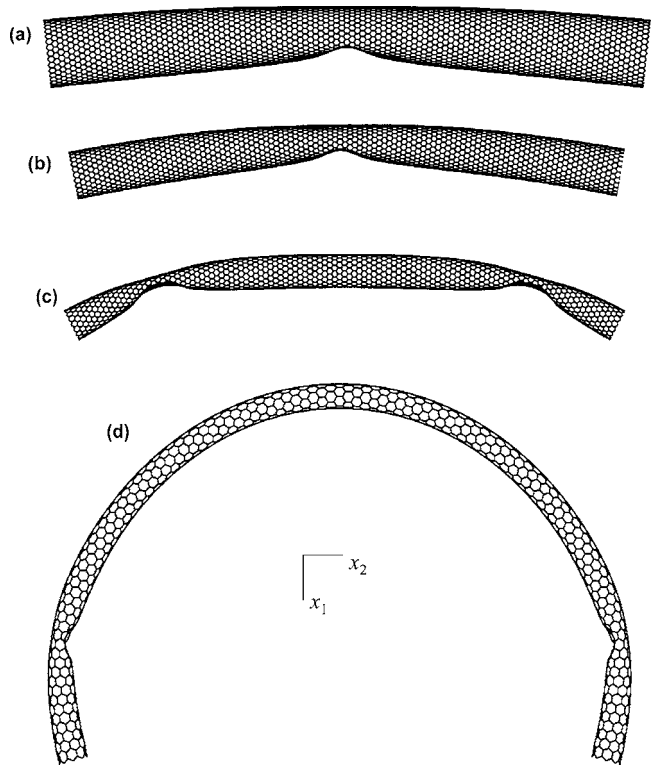

FIG. 6. The geometry of zigzag tubes at the onset of bending buckling with fixed length (L=24 nm) and different radii: (a) (35,0), (b) (26,0), (c) (17,0), and (d) (9,0).

of a double-walled CNT, there is a sharp transition from a single kink in the middle to two symmetric kinks near the end. The formation of secondary kink was attributed to the excessive strain buildup caused by the mismatch in the compressive sides of the two CNT layers. Wang *et al.*[40] studied the bending instability of a double-walled tube and found that with increasing tube length, the postbuckling shape changes from only one kink at the middle to two symmetric kinks near the end. They related such phenomenon to the van der Waals interaction between two layers. However, the same buckling characteristics are also found in the SWCNTs studied in this paper, which indicate that the buckling mechanisms are not dictated by the van der Waals interaction. Instead, we propose that these phenomena may be related to the displacement boundary condition imposed during bending deformation, whose effect will be examined in the next section.

FEM simulations also show similar buckled geometries of SWCNTs, shown in Fig. 7 for a (10,10) tube with fixed wall thickness (t=0.066 nm) and different lengths. If the aspect ratio L/d is small, the buckled shape has one kink in the middle [Fig. 7(b)], and the postbuckling shape will change to two symmetric kinks near the end with further bending. For tubes with moderately large aspect ratio, two symmetric snap buckles form near the end [Fig. 7(d)], and one extra kink will appear in the middle of tube with further deformation. In this sense, the bending buckling mechanisms of SWCNTs are similar to those of cylindrical thin shells. It is reminded that these FEM simulations provide only qualitative insights, since they fail to predict the reduction of critical bending buckling curvature when the buckled geometry is changed (Fig. 4).

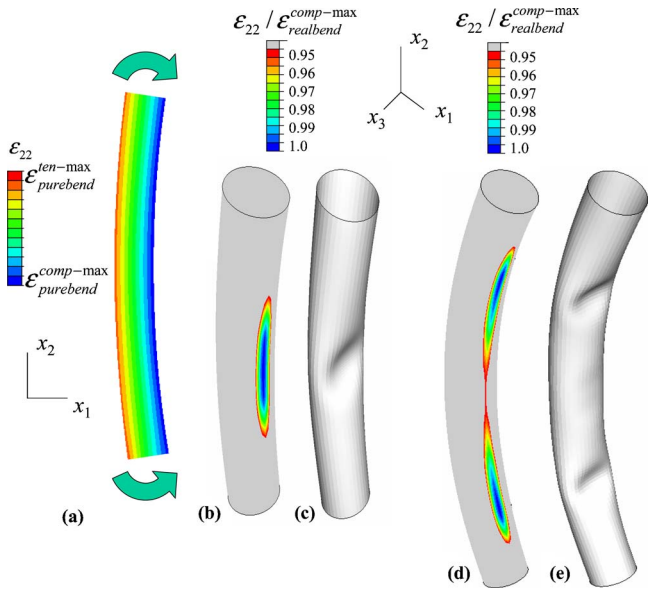

FIG. 7. (Color online) The effect of boundary condition simulated by FEM. (a) The ideal distribution of axial strain of pure bending. For (10,10) tube with L=6.2 nm and t=0.066 nm: (b) The contour plot of axial strain ε_{22} just before buckling, and (c) the subsequent buckled geometry. For (10,10) tube with L=12.5 nm and t=0.066 nm: (d) The contour plot of axial strain ε_{22} just before buckling, and (e) the subsequent buckled geometry.

D. Effect of boundary condition on bending buckling of SWCNTs

In most similar MD simulations known to the authors, bending is displacement controlled[10,15,18] which imposes rigid-body translations on the carbon atoms in both end layers, such that the end sections remain circular and perpendicular to the deformed axis. For a given bending angle, the new positions of the atoms in the end layers can be calculated by assuming that the axis deforms into an arc in x_1-x_2 plane with fixed length. Ideally, in pure bending situation, the curvature and axial strain are both uniform along the longitudinal direction; moreover, the distribution of axial strain ε_{22} (in the deformed system) is linear across the cross section, as sketched in Fig. 7(a). The maximum compressive axial strain of the entire tube is $\varepsilon_{purebend}^{comp\text{-max}}=-\kappa d/2$, which is distributed uniformly on the rightmost longitudinal line [blue in Fig. 7(a)], where κ is the curvature of deformed tube axis. Likewise, the maximum tensile ε_{22} is $\varepsilon_{purebend}^{ten\text{-max}}=\kappa d/2$ on the leftmost longitudinal line [red in Fig. 7(a)]. $\varepsilon_{purebend}^{comp\text{-max}}$ is the key for buckling when the deformation of tube is pure bending.

However, due to the displacement boundary condition imposed during the simulation, the end layers remain circular and that imposes extra constraints since the sections away from the end become elliptical during bending. Thus, the curvature (κ) and axial strain distribution (ε_{22}) are nonuniform along the longitudinal directions as a consequence of

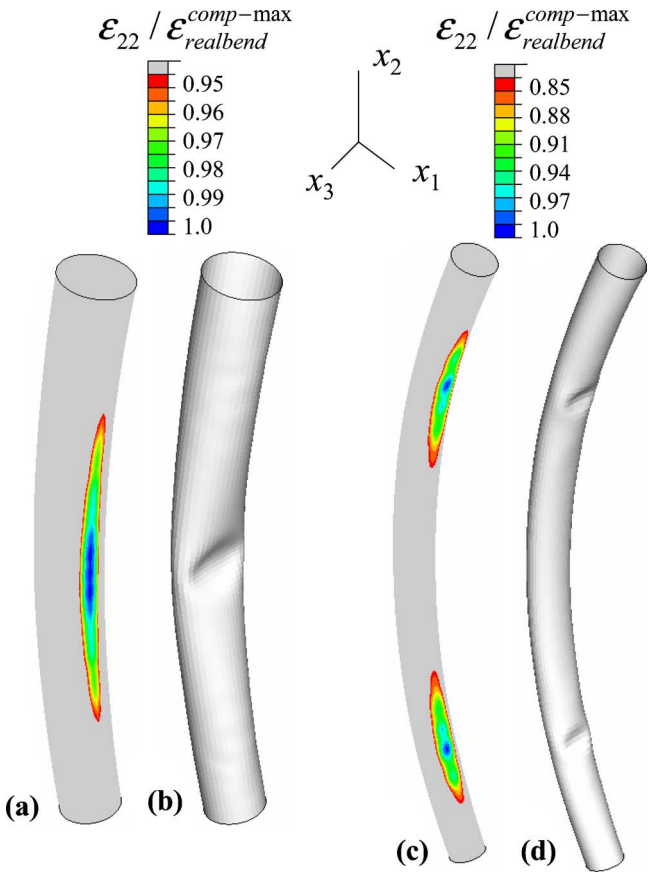

FIG. 8. (Color online) The effect of boundary condition simulated by FEM. For (20,20) tube with $L=25$ nm and $t=0.066$ nm: (a) The contour plot of axial strain ε_{22} just before buckling, and (b) the subsequent buckled geometry. For (20,20) tube with $L=50$ nm and $t=0.066$ nm: (c) The contour plot of axial strain ε_{22} just before buckling, and (d) the subsequent buckled geometry.

such boundary condition, i.e., the deformation deviates a little from pure bending. Helpful insights can be obtained from FEM simulations of cylindrical shells in bending with the same displacement boundary condition. Two examples of contour plots of the actual distribution of axial strain ε_{22} are shown in Figs. 7(b) and 7(d), respectively, for (10,10) tube with $L=6.2$ and 12.5 nm. The maximum compressive axial strain of the whole tube which occurred in practice is denoted by $\varepsilon_{realbend}^{comp\text{-max}}$: In the longer tube [Fig. 7(d)], it is apparent that near each end of the tube, the nonuniform curvature along the longitudinal directions has lead to two prominent compression zones. Subsequently, two snap buckles develop right at the symmetric locations with maximum compressive strain $\varepsilon_{realbend}^{comp\text{-max}}$ [Fig. 7(e)]. In the shorter tube, the two prominent compression zones overlap and make $\varepsilon_{realbend}^{comp\text{-max}}$, occurring right in the middle of the tube [Fig. 7(b)], which also coincides with the subsequent kink [Fig. 7(c)].

From FEM simulation, two more examples of the axial strain field and buckled geometry are given in Figs. 8(a), 8(c), 8(b), and 8(d), respectively, for (20,20) tubes with lengths 25 and 50 nm. In Fig. 8(c), the prominent compression zones are found near both ends of the tube, and the location of $\varepsilon_{realbend}^{comp\text{-max}}$ coincides with the subsequent kink [Fig. 8(d)]. Both the size of compression zone and the distance between $\varepsilon_{realbend}^{comp\text{-max}}$ and end are larger than that shown in Fig. 7(d); thus, the size and location of the prominent compression zone scales with the tube radius. Same characteristics are observed in Figs. 8(a) and 8(b). The effect of displacement boundary condition becomes larger for tubes with larger radii.

For a SWCNT with given chirality and length, there are two main questions for bending buckling: (1) where is the location of kink? and (2) what is the critical condition for bending buckling?

(1) In all cases, the location of the kink is dominated by the local maximum compressive axial strain found in practice, $\varepsilon_{realbend}^{comp\text{-max}}$. At that point, snap buckle occurs with respect to the long axis of the deformed elliptical cross section, which has a smaller moment of inertia compared with the short axis.

(2) The exact critical state for bending buckling is affected by the actual distribution of strain field components, including both axial and hoop strains, which are consequences of the boundary condition. An exact bifurcation solution of a tube with the aforementioned displacement boundary conditions is complicated and unnecessary. Instead, a *phenomenological* threshold is established on the equivalent pure bending configuration: the bending buckling occurs once $\varepsilon_{purebend}^{comp\text{-max}}$ in the equivalent pure bending configuration reaches a critical value—the critical bending buckling strain is described as ε_c^{FEM} in the continuum model and ε_c in MD analyses. Thus, ε_c^{FEM} or ε_c do not exactly equal the maximum axial compressive strain observed in practice. This phenomenological formulation is proven effective and consistent with the literature.

IV. CONCLUSION

In this paper, extensive MD analyses are carried out to investigate the buckling behaviors of SWCNTs under bending deformation. Explicit relationships are established between the critical bending buckling curvature and the geometry parameters of SWCNTs, such as tube diameter, length and chirality, and the results are correlated with the buckled geometry. In addition, parallel FEM simulations based on the continuum shell model are also used to study the bending buckling characteristics of SWCNTs. Critical insights into the buckling mechanisms, critical buckling strain of bending versus axial compression, and the effects of boundary condition are obtained. Improvements on continuum modeling are suggested.

When the SWCNT length is fixed, the critical bending buckling curvature decreases as inverse square of the tube diameter (Fig. 1), and the critical bending buckling strain is proportional to the inverse of the tube diameter (Fig. 2). These results are not sensitive to the chirality of tube. Similar diameter dependence is observed in FEM simulations, although the computed critical bending buckling curvature is larger than that found in MD studies. Such difference is caused by the geometrical imperfections in MD simulations (which is an intrinsic characteristic of the CNT) during the minimization of atomic system potential energy. The onset of buckling is very sensitive to imperfections, which reduces

the critical buckling load. Thus, the critical bending buckling strain (or curvature) of the imperfection-free shell model in FEM analyses is much higher than that of an imperfection-containing structure used in MD simulations (Figs. 1 and 2). On the other hand, the overall effect of geometrical imperfections in MD simulations can be represented by either a correction factor or an effective shell thickness, which makes the critical bending buckling curvature computed from FEM agree with MD.

In the continuum model, the critical bending buckling curvature is essentially independent of the tube length (Fig. 4). Whereas, in MD simulations (Fig. 3) it is found that when the tube aspect ratio is less than a threshold value, there is a sharp reduction of critical bending buckling curvature. The threshold aspect ratio is slightly larger and the critical curvature reduction becomes smaller for tubes with larger radii. From postbuckling geometries of MD simulations (Figs. 5 and 6), it is found that such threshold is related to the transition of buckled geometry: below the threshold aspect ratio only one kink is found in the middle of the tube, and above such threshold two symmetric kinks develop near the end of the tube. Similar trend has been observed in FEM simulation (Figs. 7 and 8), yet the transition of buckled shape does not agree with MD simulation, and variation of critical bending buckling curvature is not obvious with such transition.

Although FEM simulations are phenomenological and qualitative in many aspects, they provide critical insights into several key issues for bending buckling of SWCNTs: (1) the key relationships $\kappa_c \sim 1/d^2$ and $\varepsilon_c \sim 1/d$ hold for most tubes investigated by MD simulations, except for those with very small aspect ratios and of less practical value. (2) The FEM buckled geometry (Figs. 7 and 8) qualitatively agree with MD simulation (Figs. 5 and 6), where the number of kinks are increased with increasing aspect ratio. (3) By comparing the critical buckling strains occurring under bending and axial compression (Fig. 2), it is confirmed that these two modes are distinct and the critical buckling strains are not equal. Therefore, the assumption that the critical bending buckling strain simply equals to critical compressive buckling strain[15] is problematic. (4) The contour plots of axial strain (Figs. 7 and 8) show that due to the displacement boundary condition imposed under bending deformation, the curvature is not as uniform as expected. Instead, at some distance away from the end, prominent compression zones are developed and the snap buckles occur subsequently right at the locations of maximum compressive axial strain. For longer tubes, the prominent compression zones are apart and they overlap for shorter SWCNTs, and the resulting prominent compression zone is larger for tubes with larger radii. Thus, the number of kinks developed during buckling, as well as their positions, are dominated by these prominent compression zones.

Without losing generality, the bending buckling behavior of SWCNTs can still be simulated as thin cylindrical shells, where the effect of geometrical imperfections on the critical bending buckling curvature may be represented by a correction factor. The studies in this paper may provide important information on the buckling mechanisms of SWCNTs, and become useful in practical applications where buckled CNTs are used in nano-electromechanical systems as nano-valves or switches.

ACKNOWLEDGMENTS

This work is supported in part by NSF Grant No. CMS-0407743, "Measurement of mechanical properties of small material structures by nanoindentation" (Program Officer: Ken Chong), and in part by Columbia University Academic Quality Fund "Columbia Nanomechanics Research Center."

*Electronic address: xichen@civil.columbia.edu

[1] H. Dai, J. H. Hafner, A. G. Rinzler, D. T. Colbert, and R. E. Smalley, Nature (London) **384**, 147 (1996).
[2] P. Kim and C. M. Lieber, Science **286**, 2148 (1999).
[3] P. Pancharal, Z. L. Wang, D. Ugarte, and W. de Heer, Science **283**, 1513 (1999).
[4] S. J. Tans, R. M. Verschueren, and C. Dekker, Nature (London) **393**, 49 (1999).
[5] R. S. Friedman, M. C. McAlpine, D. S. Ricketts, D. Ham, and C. M. Lieber, Nature (London) **434**, 1085 (2005).
[6] M. M. J. Treacy, T. W. Ebbesen, and J. M. Gibson, Nature (London) **381**, 678 (1996).
[7] A. Krishnan, E. Dujardin, T. W. Ebbesen, P. N. Yianilos, and M. M. J. Treacy, Phys. Rev. B **58**, 14013 (1998).
[8] E. W. Wong, P. E. Sheehan, and C. M. Lieber, Science **277**, 1971 (1997).
[9] P. Poncharal, Z. L. Wang, D. Ugarte, and W. A. de Heer, Science **283**, 1513 (1999).
[10] S. Iijima, C. Brabec, A. Maiti, and J. Bernholc, J. Chem. Phys. **104**, 2089 (1996).
[11] M. R. Falvo, G. J. Clary, R. M. Taylor, V. Chi, F. P. Brooks, Jr., S. Washburn, and R. Superfine, Nature (London) **389**, 582 (1997).
[12] T. W. Tombler, C. W. Zhou, L. Alexseyev, J. Kong, H. Dai, L. Liu, C. S. Jayanthi, M. J. Tang, and S. Y. Wu, Nature (London) **405**, 769 (2000).
[13] H. W. C. Postma, T. Teepen, Z. Yao, M. Grigoni, and C. Dekker, Science **293**, 76 (2001).
[14] M. Grujicic, G. Cao, B. Pandurangana, and W. N. Royb, Mater. Sci. Eng., B **117**, 53 (2005).
[15] B. Yakobson, C. J. Brabec, and J. Bernholc, Phys. Rev. Lett. **76**, 2511 (1996).
[16] K. M. Liew, C. H. Wong, X. Q. He, M. J. Tan, and S. A. Meguid, Phys. Rev. B **69**, 115429 (2004).
[17] M. J. Buehler, Y. Kong, and H. Gao, Mater. Sci. Technol. **126**, 246 (2004).
[18] P. Liu, Y. W. Zhang, C. Lu, and K. Y. Lam, J. Phys. D **37**, 2358 (2004).
[19] T. Belytschko, S. P. Xiao, G. C. Schatz, and R. S. Ruoff, Phys. Rev. B **65**, 235430 (2002).
[20] M. B. Nardelli, B. I. Yakobson, and J. Bernholc, Phys. Rev. Lett. **81**, 4656 (1998).
[21] T. Ozaki, Y. Iwasa, and T. Mitani, Phys. Rev. Lett. **84**, 1712

(2000).
[22] D. Srivastava and S. Barnard, *Molecular Dynamics Simulation of Large-Scale Nanotubes on a Shared-Memory Architecture* (ACM Press, New York, 1997).
[23] A. Pantano, M. C. Boyce, and D. M. Parks, Phys. Rev. Lett. **91**, 145504 (2003).
[24] A. Pantano, D. M. Parks, and M. C. Boyce, J. Mech. Phys. Solids **52**, 789 (2004).
[25] C. Q. Ru, J. Mech. Phys. Solids **49**, 1265 (2001).
[26] M. Arroyo and T. Belytschko, Phys. Rev. Lett. **91**, 215505 (2003).
[27] X. Q. He, S. Kitipornchai, and K. M. Liew, J. Mech. Phys. Solids **53**, 303 (2005).
[28] X. Chen and G. Cao, Nanotechnology **17**, 1014 (2006).
[29] T. Xiao, X. Xu, and K. Liao, J. Appl. Phys. **95**, 8145 (2004).
[30] C. Q. Ru, Phys. Rev. B **62**, 9973 (2000).
[31] T. Chang, G. Li, and X. Guo, Carbon **43**, 287 (2003).
[32] T. Chang, W. Guo, and X. Guo, Phys. Rev. B **72**, 064101 (2005).
[33] C. Y. Li and T. W. Chou, Mech. Mater. **36**, 1047 (2004).
[34] H. Sun, P. Ren, and J. R. Fried, Comput. Theor. Polym. Sci. **8**, 229 (1998).
[35] A. Libai and J. G. Simmons, *The Nonlinear Theory of Elastic Shells* (Cambridge University Press, Cambridge, 1998).
[36] ABAQUS, *ABAQUS 6.4 User's Manual* (ABAQUS, Pawtucket, RI, 2004).
[37] X. Zhou, J. J. Zhou, and Z. C. Ou-Yang, Phys. Rev. B **62**, 13692 (2000).
[38] Z. C. Tu and Z. C. Ou-Yang, Phys. Rev. B **65**, 233407 (2002).
[39] K. N. Kudin, G. E. Scuseria, and B. I. Yakobson, Phys. Rev. B **64**, 235406 (2001).
[40] Q. Wang, T. Hu, G. Chen, and Q. Jiang, Phys. Rev. B **71**, 045403 (2005).